ARTICLE

Marked Thermal Exaltation in Hybrid Thin Membranous Nanomaterials Covered by Stretched Nanodots for Thermoelectrics and Passive Cooling

Jean-Numa Gillet*

University of Lille 1, Department of Physics, Cité scientifique, 59655 Villeneuve d'Ascq cedex, France

ABSTRACT An anisotropic thin membranous nanomaterial is modeled at the molecular scale to obtain a hybrid thermal behavior with applications from thermoelectrics to passive heat sinking. These antagonist phenomena, with different heat carriers, are obtained in two orthogonal in-plane directions, respectively x and y, when the thin membrane is covered by stretched nanodots forming elongated islands parallel to y. The phonon thermal conductivity is minimal in the direction x but maximal in that y. In nanomaterials composed of Si and Ge for the membrane and islands, respectively, thermal-conductivity exaltation as high as 22 folds is computed between the two phonon regimes in this theoretical study.

KEYWORDS: molecular modeling • clean-energy materials • thermoelectrics • thermal nanostructures • interface properties • cross-disciplinary applied materials

INTRODUCTION

A thin membrane, covered by elongated nanodots with another composition, is modeled at the molecular scale to generate for the first time a hybrid thermal behavior between insulation and passive dissipation of the phonon heat carriers from a symmetry break. Cooling from two physical phenomena of different natures is obtained using the same materials nanostructure, when hot and cold junctions are connected with respect to two orthogonal directions x and y. If the two junctions are linked through the elongation direction y of the stretched nanodots, forming a network of parallel islands at the top of a membrane face, passive heat sinking from the wave-guided phonons is maximal with the highest lattice thermal conductivity λ in the nanostructure. In contrast, when the junctions are connected with respect to the orthogonal in-plane direction x, from which the smallest width of the islands is observed, phonon transport is blocked leading to the lowest λ in the nanostructure. On-demand thermoelectric Peltier cooling from electrons or holes can therefore be generated in the direction x by switching on an electrical current between the junctions. Marked thermal-conductivity exaltation is obtained between the two opposite thermal regimes related to the directions x and y.

In this theoretical study, the hybrid nanomaterial is made up of a thin diamond-cubic (dc) Si membrane covered by elongated domelike Ge nanodots with epitaxy facets. Such a design can be synthesized with IV−IV self-assembly technologies as those based on MBE (molecular beam epitaxy) (1−6). CVD (chemical vapor deposition) processes can also be envisioned to synthesize the proposed nanomaterial (7). As sketched in Figure 1, the Ge nanodots are voluntarily stretched to form elongated islands in the direction [010] or y, parallel to the membrane, whereas they are observed as shrunk in the orthogonal in-plane direction [100] or x. The anisotropic λ, analyzed vs the crystallographic directions $\mathbf{r}$ in a membrane plane, can be smaller than the lowest limit ($\sim$1 W m^{-1} K^{-1}) of bulk amorphous Si when $\mathbf{r} = \mathbf{x}$. This first phonon thermal regime is insulating and useful for thermoelectric Peltier cooling as well as Seebeck generation. Differently, λ is significantly exalted by a factor that can be larger than 22 folds when $\mathbf{r} = \mathbf{y}$ instead of $\mathbf{r} = \mathbf{x}$. This second thermal behavior is dissipative for the phonons. Applications from thermoelectrics (small λ) to passive heat sinking (high λ) can therefore be envisioned using the same materials nanostructure. The thin nanostructure can be generalized to other compounds pairs as those based on III−V or II−VI semiconductors. Ge and Si are, however, emphasized in this paper because they show an indirect electronic band gap resulting in a negligible electronic thermal conductivity $\lambda_e \approx 0$. Indeed, the thermoelectric figure of merit ZT depends on $1/\lambda$. The relatively high λ_e value of semiconductors with a direct electronic band gap would therefore result in an adverse effect on the possible ZT decrease because of a low lattice thermal conductivity.

ZT is computed as $ZT = S^2\sigma T/\lambda$, where S, σ, T, and λ are the Seebeck coefficient, electrical conductivity, temperature, and thermal conductivity, respectively (8−13). ZT is directly proportional to the power factor $S^2\sigma$ but inversely proportional to λ. $ZT \geq 3$ would produce a thermoelectric yield higher than 42% of the Carnot efficiency for hot and cold junctions at 800 and 300 K, respectively. This value is in the

* Corresponding author. E-mail: jngillet@gmail.com.
Received for review July 26, 2010 and accepted November 8, 2010
DOI: 10.1021/am1006518

Published on Web 11/24/2010

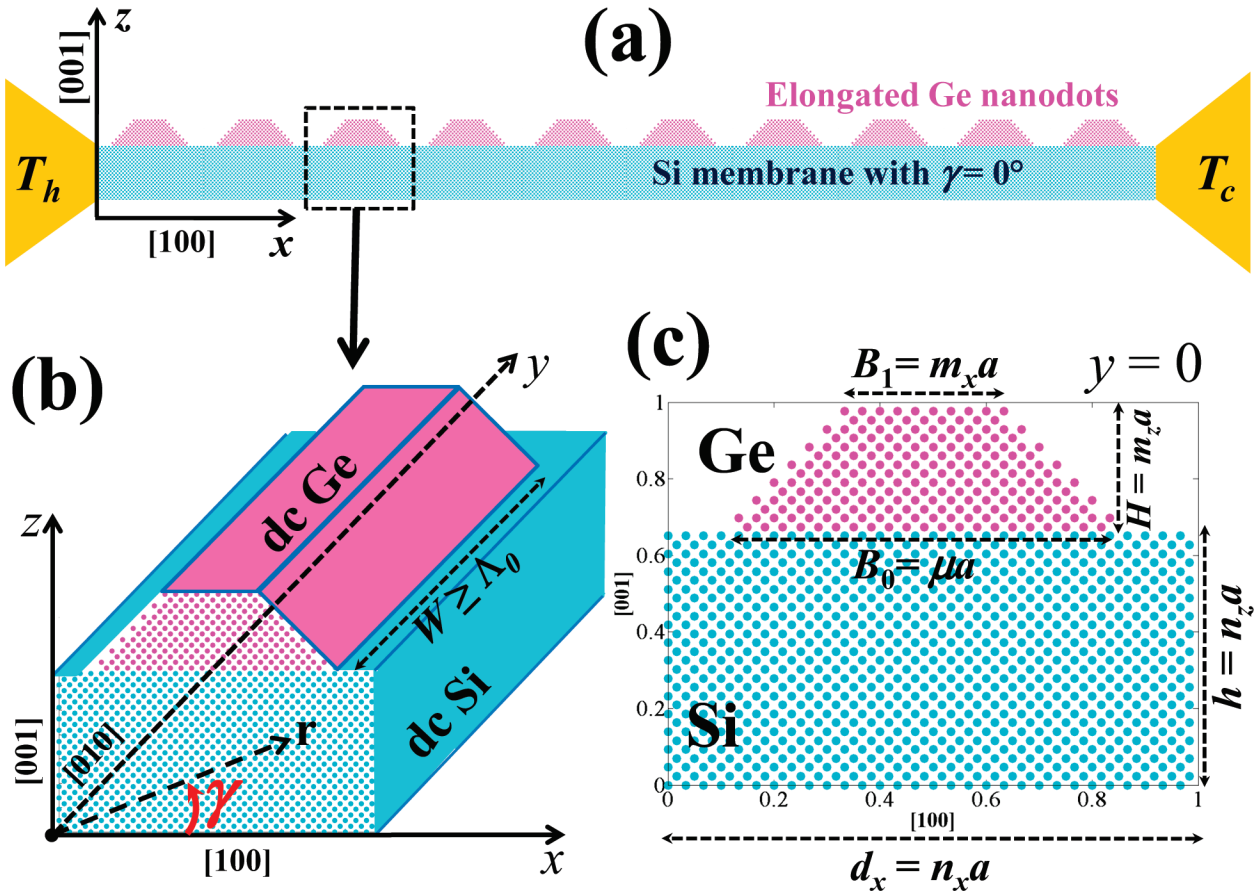

FIGURE 1. Thin nanomaterial: Cyan and magenta balls represent Si and Ge atoms, respectively. (a) Nanomaterial section displayed in the plane (x, z). Two lateral membrane sides are assumed to be cleaved along two planes with the Miller indices (010). When junctions with hot (T_h) and cold (T_c) temperatures are connected to the other orthogonal sides, the heat flux propagates in [100] related to $\gamma = 0°$, corresponding to the shrinking direction of the Ge islands. (b) 3D zoom of a repetitive nanomaterial unit presented in panel a. The Ge island is stretched along [010] with a length $W \geq \Lambda_0$. An angle γ is defined in a membrane plane (x, y) from the axis x. When the heat flux propagates (following r) with either $\gamma = 0°$ or $\gamma = 90°$, the anisotropic thermal conductivity λ is either minimal or maximal, respectively. (c) Section with the coordinate $y = 0$ of the repetitive unit. The integer size parameters, given by $n_x = 30$, $n_z = 14$, $m_x = 9$, $m_z = 7$, and $\mu = 21$, are those in "Template 1". They are related to the respective (nonrelaxed) lengths $d_x = 16.293$ nm, $h = 7.603$ nm, $B_1 = 4.88$ nm, $H = 3.802$ nm, and $B_0 = 11.405$ nm.

range of the yields of conventional thermal engines. A high ZT would therefore lead to major progresses in green energy. Superlattices with periodic thin layers were studied to obtain $ZT > 1$ because of phonon confinement between their layers. Their synthesis with ZT higher than unity is however tricky due to lattice mismatches forming dislocations and cracks. Nanowires were as well proposed for λ diminution. Unfortunately, as the superlattices, they decrease λ in only one propagation direction. In experiments, these quasi one-dimensional (1D) insulating materials usually fail to beat the lowest limit of amorphous Si around 1 W m^{-1} K^{-1}. Three-dimensional (3D) self-assembled arrays of Ge quantum dots in Si were made by epitaxy for quantum-electronic and photovoltaic devices (1, 2). Theoretical studies of 3D supercrystals made up of Ge quantum dots in Si were recently proposed to design thermoelectric materials (8−11). An extreme reduction of the thermal conductivity with a value equal or lower than that of air (~0.025 W/m/K) was predicted in these Si−Ge supercrystals for a broad temperature range ($T \leq 1200$ K) using different size parameters and Ge concentrations (8−10). A high ZT could therefore be achieved in these Si−Ge supercrystals (because ZT is inversely proportional to λ).

The presented research could lead to nanoengineering applications: Semiconducting-nanomaterial design with an indirect electronic band gap is currently challenging to obtain an optimal thermal transport for energy conversion and on-chip cooling in nanoscale silicon-based architectures. Indeed, continuation of the Moore's law in CMOS (complementary-metal-oxide-semiconductor) microelectronics is currently failing due to thermal problems from undesired thermal budget, hot spots, transistor-gate leakage or high power dissipation (13−15). On the other hand, performance of miniaturized biochips and laboratories-on-a-chip also depend on the temperature resulting in thermal drawbacks. Indeed, they can be composed of heating parts as PCR (polymerase chain reaction) microchambers or microfluidic reactors (16−18).

MODEL SECTION

In the proposed membranous nanomaterial, the epitaxial-growth direction [001] of the nanodots is denoted as z. The latter is perpendicular to the membrane, as shown in Figure

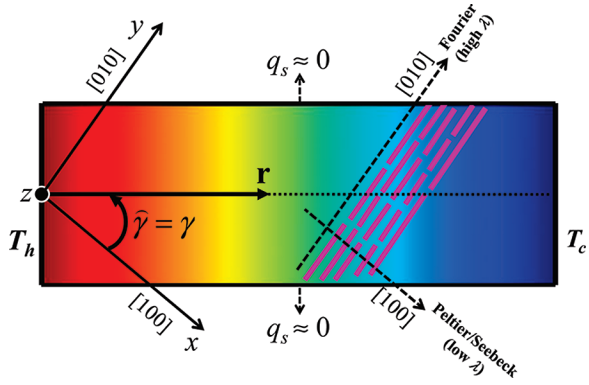

FIGURE 2. Schematic top view of the thin nanomaterial presenting the boundary conditions used to obtain heat propagation according to r. The Ge islands are stretched in the direction *y* while their bases are the smallest in that *x*, from which is defined an angle γ between 0° (*x*) and 90° (*y*). In the right-hand side of the scheme, five possible lines composed of Ge islands are sketched to show their stretching orientation along [010] or *y*.

1. The average length $\langle W \rangle$ of the Ge islands in [010] is defined as larger or equal to the average phonon mean free path (MFP) in bulk dc Si computed as $\Lambda_0 \approx 100$ nm at $T = 300$ K (11). In contrast, the Ge islands have a bottom basis B_0 several-fold smaller than Λ_0 in the orthogonal in-plane direction [100] [Figure 1b]. From this anisotropy, waveguiding of the phonons is obtained in [010] while their transport is blocked in [100]. To exploit these antagonist effects, as depicted in Figure 2 (schematic top view), we assumed the membrane to be cleaved at the device scale to form two boundary sides with vacuum or soft material showing a negligible normal heat flux q_s taken from the sides that are parallel to a direction **r** forming an angle γ with the Ge-island shrinking direction [100]. Because of these boundary conditions (BCs), defined in Figure 2 for a sufficiently large island number, the heat-propagation direction is given by **r** for a given γ. When two junctions with hot (T_h) and cold (T_c) temperatures are connected to the other sides of the membrane, orthogonal to **r**, the anisotropic λ is studied vs γ to show its exaltation when γ is rotated from 0 to 90°, related to the orthogonal directions [100] and [010], respectively.

The λ vs γ curve is computed using 3D lattice dynamics (11, 19) and incoherent scattering approach (20−22). Therefore, the Ge-island lengths in [010] can be different if the inequality $\langle W \rangle \geq \Lambda_0$ holds with $B_0 < \Lambda_0$, as depicted in the right-hand side of Figure 2 (schematic examples). Moreover, because $\langle W \rangle$ is significantly stretched in [010], the nonrelaxed width of a supercell used for lattice-dynamics calculations can be thinned to the Si lattice parameter $a = 0.5431$ nm in [010] as if the Ge islands were infinite in that direction for heat propagation. Consequently, as shown in Figure 3 where the cyan and magenta balls respectively depict the Si and Ge atom positions, a supercell can be defined as a slab with a width of only one interatomic distance in [010]. A discrete supercell slab is encoded at the molecular scale to obtain a finite number of phonon dispersion curves vs γ from lattice dynamics. The slopes of the dispersion curves, related to phonon group velocities, are usually much larger in [010] with respect to [100] (see Appendix to Model Section for details). As a result, λ is significantly exalted when γ is rotated from 0° to 90°. The length of a supercell is given by d_x in the shrinking direction x of the Ge islands (Figure 1c). Their top bases are denoted by B_1 in x. In the nonrepetitive direction z, the height of the Si membrane is h while that of the Ge islands is H. In agreement with the dc subgroup, only four molecular sections with the nonrelaxed coordinates $z = 0$, $z = a/4$, $z = a/2$ and $z = 3a/4$ are used to define a supercell slab (Figure 3). The slab section at $z = 0$ is displayed in Figure 1c. The space domain is quantized with the interatomic lattice constant a. The nonrelaxed lengths $d_x = n_x a$, $h = n_z a$, $B_1 = m_x a$, $H = m_z a$, and $B_0 = \mu a$ are obtained from the integer size parameters n_x, n_z, m_x, m_z, and μ, respectively. The growth facets in the island slab are assumed to show a 45° deflection angle with respect to the x and z axes (Figure 1c). Hence, the reduced bottom basis μ of a Ge island must respect the equality $\mu = 2(m_y - 1) + m_x$.

The anisotropic thermal conductivity $\lambda(\gamma)$ is computed for a given γ between 0 and 90° (see the Supporting Information, Part A, for the details) using

$$\lambda(\gamma) = \int_0^{\pi/2} [\cos(\gamma - \phi)]^2 P_1(\phi) d\phi + \int_0^{\pi/2} [\sin(\gamma - \phi)]^2 P_2(\phi) d\phi + \int_0^{\pi/2} \sin[2(\gamma - \phi)] P_3(\phi) d\phi \quad (1)$$

In eq 1, the three integration kernels $P_i(\phi)$ with $i = 1$, 2, and 3 depend on the only azimuthal variable ϕ in the two-dimensional (2D) reciprocal space with the polar coordinates (k, ϕ). A reciprocal space with only two dimensions is considered because there is no repetition of the thin nanomaterial in z. $P_1(\phi)$ and $P_2(\phi)$ are functional of the square of the radial $[v_m(k,\phi)]$ and azimuthal $[v_m(k,\phi)]$ group velocities of the phonons in the first 2D Brillouin zone (BZ). In contrast, $P_3(\phi)$ is functional of the product $u_m(k,\phi) \times v_m(k,\phi)$. The kernels $P_i(\phi)$ are also related to the scattering relaxation times $\tau_m(k,\phi)$ of the phonon eigenmodes indexed by m. These average life times are obtained from an incoherent approach where the non-normalized scattering probability is given by $[\tau_m(k,\phi)]^{-1} = [\tau_m^{(u)}(k,\phi)]^{-1} + [\tau_m^{(s)}(k,\phi)]^{-1}$. In this expression, $\tau_m^{(u)}(k,\phi)$ denotes the umklapp relaxation times (11, 23). The other scattering mechanisms are described by the relaxation times $\tau_m^{(s)}(k,\phi)$. To compute their values, only interface scattering is considered in the direction z. They can be derived from the interface backscattering cross section as

$$1/\tau_m^{(s)}(k,\phi) = V_m(k,\phi)/\langle l \rangle \text{ with } \langle l \rangle \approx h + \alpha H \text{ for the constant } \alpha \leq 1 \quad (2)$$

In eq 2, $\langle l \rangle$ denotes the average phonon MFP and $V_m(k,\phi) = \{[u_m(k,\phi)]^2 + [v_m(k,\phi)]^2\}^{1/2}$ is the phonon group-velocity amplitude in a membrane plane (x, y). Because of significant band-structure folding, the phonon modes in the "optical" branches of a 2D dispersion diagram related to a defined ϕ have folded wavelengths smaller than the nanostructure characteristic lengths. Moreover, for the three "acoustical"

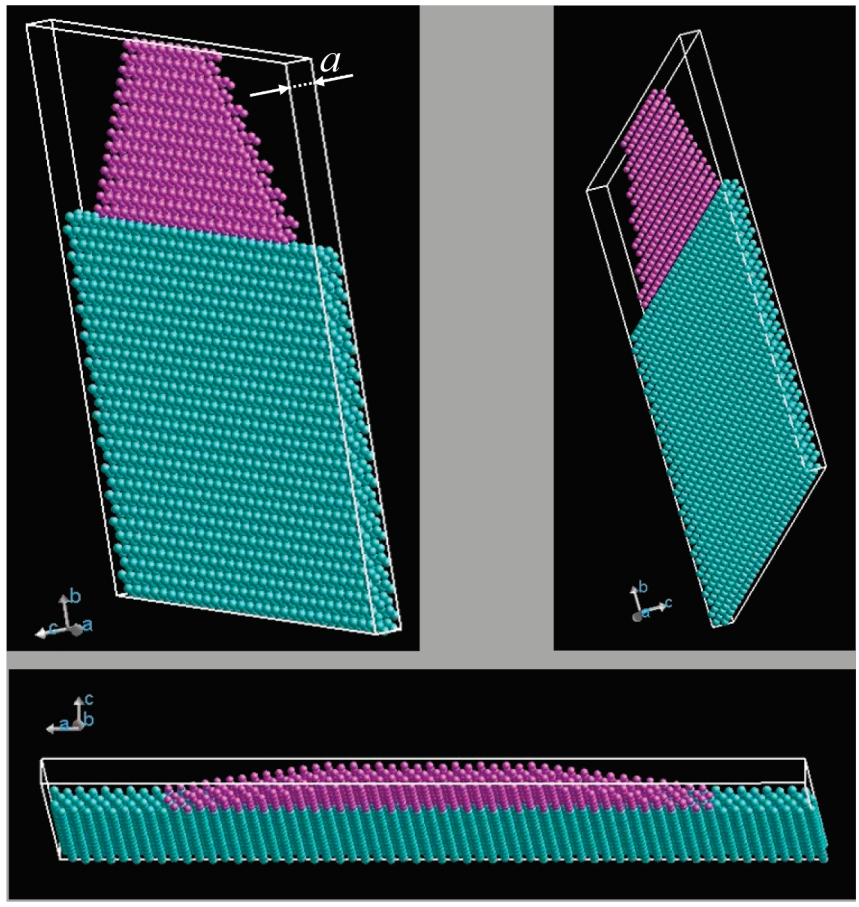

FIGURE 3. Supercell slab of "Template 1" with a nonrelaxed width $a = 0.5431$ nm in the direction y (3D views). 3480 Si atoms and 868 Ge atoms (out of a total number of 4348) are respectively colored in cyan in the slab of the Si membrane and magenta in that of the Ge elongated island.

branches, only the modes with larger wavenumbers give a thermal-transport contribution since far-field scattering is nonsignificant (10, 11, 22). Also, a supercell of the nanomaterial sketched in Figure 3 is made up of 4348 atoms leading to $3 \times 4348 = 13044$ dispersion curves for a given ϕ. Thus, the three "acoustical" curves fill only $3/13044 \times 100 = 0.02\%$ of a 2D dispersion diagram. From the precedent, near-geometrical approaches, as those derived by van de Hulst, can be used to calculate $\langle l \rangle$ from an analogy with optics (20−22). Backscattering can therefore be considered as the predominant mechanism to obtain $\langle l \rangle$ because of the BCs presented in Figure 2 (see the Supporting Information, Part B, for the details).

RESULTS AND DISCUSSION

λ is analyzed in three chosen nanomaterials (Templates "1", "2" and "3") with different geometrical parameters. Figure 3 presents a supercell of "Template 1" with the integer size parameters $n_x = 30$, $n_z = 14$, $m_x = 9$, $m_z = 7$, and $\mu = 21$. These parameters are respectively related to $d_x = 16.293$ nm, $h = 7.603$ nm, $B_1 = 4.888$ nm, $H = 3.802$ nm, and $B_0 = 11.405$ nm (Figure 1c). The total number of atoms in a "Template 1" supercell is of 4348. Among them, 3480 Si atoms are in the slab of the membrane and 868 Ge atoms in that of the island. A second nanomaterial ("Template 2") with the same thickness scaling ratio $H/h = m_z/n_z = 1/2$ than that of "Template 1" is studied but with smaller size parameters $n_x = 20$ ($d_x = 10.862$ nm), $n_z = 4$ ($h = 2.172$ nm), $m_x = 5$ ($B_1 = 2.716$ nm), $m_z = 2$ ($H = 1.086$ nm), and $\mu = 7$ ($B_0 = 3.802$ nm). These values correspond to a total number of atoms per supercell equal to 824 (including 720 Si atoms and 104 Ge atoms). A third nanomaterial ("Template 3") with the same n_x, n_y, and m_x as those used in a "Template 2" supercell is analyzed but with a larger unity thickness ratio. As a result, the other parameters $m_z = 4$ ($H = 2.172$ nm) and $\mu = 11$ ($B_0 = 5.974$ nm) are larger in "Template 3" and the total number of atoms is increased to 992 per supercell in "Template 3" compared with "Template 2".

The thermal conductivity $\lambda(\gamma)$ is analyzed vs γ at $T = 300$ K. For "Template 1" (Figure 3), a low $\lambda(\gamma)$ varying from only 1.51 to 2.94 W/m/K is computed when γ is increased from 0° to 10.3°, respectively, as shown by the top solid curves in Figure 4. Thus, the nanomaterial shows a thermal insulating behavior when $\gamma \leq 10°$. Second, when γ is augmented from 10.3 to 90°, the nanomaterial becomes efficient for passive heat sinking because the $\lambda(\gamma)$ sigmoid curve presents a large increase from 2.94 to 33.46 W m^{-1} K^{-1}, respectively. The transition between the insulating and dissipative phonon behaviors is obtained when $\gamma = 45°$ (membrane close-packed directions). In "Template 1", a marked exaltation factor of 22.1 folds is computed for $\lambda(\gamma)$ when γ is rotated

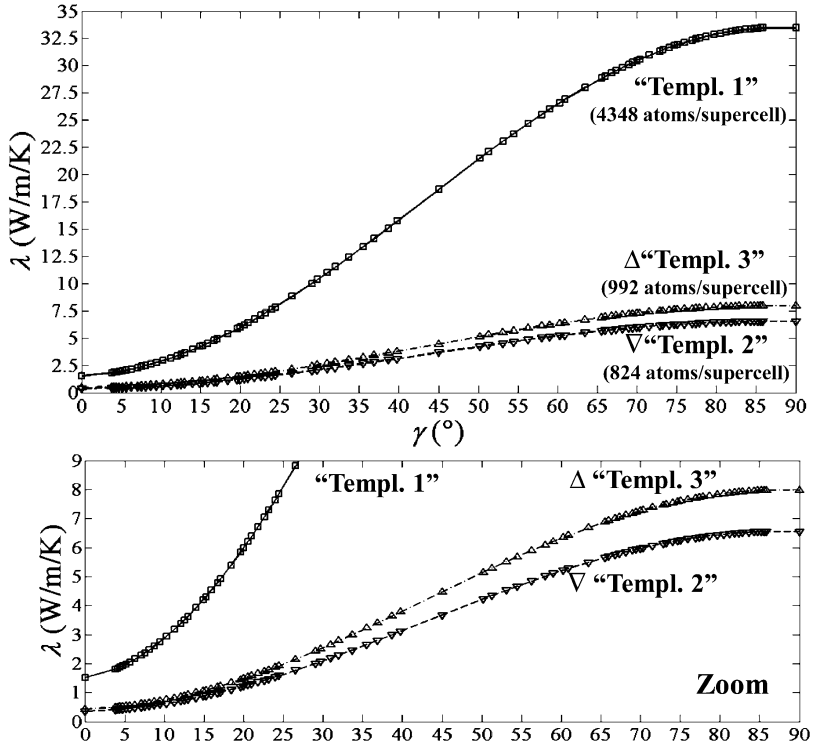

FIGURE 4. Thermal conductivity λ vs γ for Templates "1" (solid curves), "2" (dashed curves), and "3" (dashed-dotted curves). A zoom between 0 and 9 W m^{-1} K^{-1} is given in the figure bottom. Crystallographic directions of heat propagation between $\gamma = 0°$ and $\gamma = 90°$ are denoted by squares, downward triangles, and upward triangles for the Templates "1", "2", and "3", respectively.

from 0 to 90°. In y, the thermal conductivity $\lambda(90°) = 33.46$ W m^{-1} K^{-1} is only 4.5-fold smaller than that of bulk dc Si (150 W m^{-1} K^{-1}), whereas the membrane has a thickness h of only 7.6 nm.

In a thermoelectric material, the maximum pumping heat flux q_{max} is obtained as $q_{max} = 0.5\alpha^2\sigma T_c^2/L - \lambda(T_h - T_c)/L$, where L is the distance between hot and cold junctions with respective temperatures T_h and T_c (24). The first term $q_a = 0.5\alpha^2\sigma T_c^2/L$ represents the active cooling capability from the Peltier effect using electrons or holes as heat carriers. The latter is predominant with $q_{max} \approx q_a$ when λ and ZT are sufficiently small and large, respectively. The maximum heat flux q_a can be delivered on-demand when an electrical current is switched on through the material with an electrical conductivity σ. In "Template 1", the thermal conductivity in x ($\gamma = 0°$) is computed as $\lambda(0°) = 1.51$ W m^{-1} K^{-1}. This value is approximately the same than that around 1.2 W/m/K, which was experimentally measured in Bi_2Te_3-based superlattices resulting in an active cooling swing as high as $\Delta T = 9.6$ K (13). The second contribution $q_p = -\lambda(T_h - T_c)/L$ denotes the passive cooling capability from the Fourier effect due to the phonons. The latter is predominant when λ is sufficiently large leading to $q_{max} \approx q_p$. In "Template 1", λ reaches the high value $\lambda(90°) = 33.46$ W m^{-1} K^{-1} in y. Consequently, when junctions are connected with $\gamma \approx 90°$ (instead of 0°), the same hybrid nanostructure can also provide significant passive heat dissipation using, in this case, phonons as heat carriers (instead of electrons or holes).

To emphasize phonon localization on λ, Templates "2" and "3" are modeled from supercells with several-fold smaller numbers of atoms (respectively 824 and 992) in comparison with "Template 1". In x, $\lambda(0°)$ in "Template 2" is as tiny as 0.35 W/m/K, as shown by the bottom dashed curves in Figure 4, which is useful for both Peltier and Seebeck effects. In contrast, when γ is rotated by 90°, λ is exalted to reach in y the value $\lambda(90°) = 6.56$ W m^{-1} K^{-1}, which is 5.1 fold lower than that in "Template 1". Indeed, the thicknesses h and H are 3.5-fold smaller in "Template 2". Phonon localization is less enhanced in "Template 3". Indeed, the total number of atoms is augmented by 168 Ge atoms per supercell in "Template 3" with respect to "Template 2". In "Template 3″, $\lambda(0°)$ and $\lambda(90°)$ have the respective values of 0.42 and 7.98 W m^{-1} K^{-1} when γ is increased from 0 to 90°, as shown by the middle dashed-dotted curves in Figure 4. Hence, the anisotropic thermal conductivities of Templates "1", "2", and "3" have marked exaltation factors obtained in a narrow range of 22.1, 18.6, and 18.9 fold, respectively.

CONCLUSION

A nanomaterial made up of a thin membrane covered by stretched nanodots forming elongated islands is proposed to obtain a hybrid thermal behavior that is either insulating or dissipative for the phonons. Applications ranging from thermoelectrics (small λ) to passive heat sinking (large λ) can be envisioned with the same materials nanostructure using two orthogonal directions for heat propagation, respectively x and y. When the thin membrane and asymmetric islands are respectively composed of Si and Ge, a marked exaltation factor, larger than 22 folds, is computed for the anisotropic $\lambda(\gamma)$ by rotation of γ from 0° (x) to 90° (y). The hybrid nanomaterial presents a radically different thermal behavior

with respect to other nanostructures as superlattices, antidot membranes or nanowires. (12, 13, 19, 25) A superlattice leads to a thermal-conductivity decrease only in the direction z orthogonal to its thin layers while the definition of a thermal conductivity is not relevant in any section parallel to the layers. The thermal conductivity in a (x, y) section parallel to an antidot membrane shows similar decreases in x and y. Indeed, the antidot diameters are of the same order of magnitude in x and y. A thin or rough nanowire behaves as a quasi 1D material and presents a physical thermal conductivity only according to its longitudinal axis.

APPENDIX TO MODEL SECTION

Dispersion Diagram. Because the thin nanostructure is not repeated in z, phonon dispersion curves are not physical in the corresponding reciprocal direction k_z of the 3D reciprocal space (k_x, k_y, k_z). Moreover, because of the low dimensionality of the height parameters h and H, the phonons are significantly confined in z. Therefore, only the phonon modes in the 2D reciprocal space (k_x, k_y) are considered to obtain λ vs γ. To compute the dispersion diagram, polar coordinates (k, ϕ), defined from the origin point $\mathbf{k} = 0$, are preferred over Cartesian coordinates (k_x, k_y) in the 2D reciprocal space, as shown in Figure 5. Indeed, the phonon eigenfrequencies $\omega_m(\mathbf{0})$ are obtained at the origin $\mathbf{k} = 0$ of the reciprocal space (where m is integer). Consequently, for numerical convergence, the dispersion curves are computed from the radial $k = 0$ to $K(\phi)$, where $K(\phi)$ is the distance between the origin $\mathbf{k} = 0$ and boundary of the first 2D BZ for a given ϕ. Next, the azimuthal ϕ is rotated from 0 to 90° to scan the full 3D dispersion diagram (ω_m, k, ϕ). Only the phonon modes in the top-right quarter of the first 2D BZ (where ϕ varies from 0° to 90°) are necessary due to axial symmetries with respect to k_x and k_y (Figure 5). Similar approaches enabled us to solve eigenvalues' problems with the finite-element method to obtain, for instance, 3D dispersion diagrams of 2D photonic crystals. To compute the 3D dispersion diagram, the limits of the top-right quarter of the first 2D BZ are given by $K_x = \pi/d_x$ and $K_y = \pi/a$ in the reciprocal directions k_x and k_y, respectively. Because $K_y/K_x = n_x$, the 2D BZ is therefore rectangular and elongated by a factor of n_x folds in the direction k_y with respect to that k_x (Figure 5). As a result, the rectangular BZ is stretched in k_y by factors $n_x = 30$ for "Template 1" and $n_x = 20$ for Templates "2" and "3".The dispersion curves for a given $\phi = 0°$ (direction k_x with coordinate $k_y = 0$) are flat leading to low radial group velocities $u_m(k, 0)$, as shown in Figure 6a for "Template 1". In contrast, for a given $\phi = 90°$ (direction k_y with coordinate $k_x = 0$), the radial group velocities $u_m(k, \pi/2)$ are usually higher than those obtained for $\phi = 0°$ since the dispersion curves have larger slopes than those for $\phi = 0°$, as drawn in Figure 6b. Also, the energies $\hbar\omega_m(k,\phi)$ of the phonon modes with lower eigenfrequencies can be several-fold larger when $\phi = 90°$ with respect to $\phi = 0°$ for the same

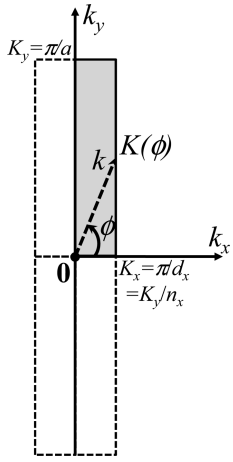

FIGURE 5. First 2D Brillouin zone to compute the 3D dispersion diagram with lattice dynamics using the reciprocal polar-coordinate system (k, ϕ). The rectangular zone is stretched by n_x folds in the reciprocal direction k_y ($\phi = 90°$) with respect to that k_x ($\phi = 0°$).

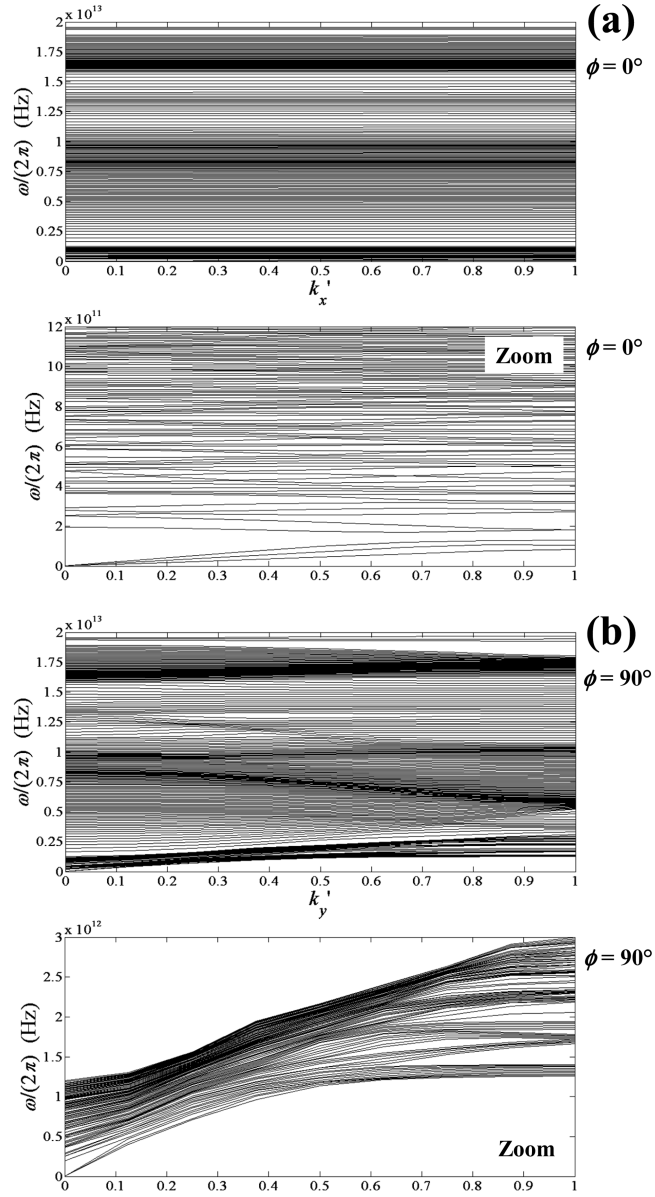

FIGURE 6. Dispersion curves of "Template 1" for given reciprocal coordinates (a) $\phi = 0°$ (direction k_x with $k_y = 0$) and (b) $\phi = 90°$ (direction k_y with $k_x = 0$). In the top diagrams in panels a and b, 210 chosen radial dispersion curves (out of a total of 13044) are plotted in a frequency range from 0 to 20 THz. The bottom diagrams in (a) and (b) are the corresponding zooms where only the first 90 dispersion curves are drawn to emphasize differences in the slopes and frequencies when $\phi = 0°$ (a) with respect to $\phi = 90°$ (b). Reduced wavenumbers are given by $k_x' = k/K_x$ and $k_y' = k/K_y$ in panels a and b, respectively.

m and k values, which can be seen by comparison of the zooms (bottom diagrams) in Figure 6(a) ($\phi = 0°$) and Figure 6(b) ($\phi = 90°$) for the first 90 dispersion curves when the reduced wavenumber grows from 0 to 1. Significant exaltation of the anisotropic thermal conductivity λ in y ($\gamma = 90°$) with respect to x ($\gamma = 0°$) is expected from evolution of the dispersion curves vs the reciprocal ϕ. Indeed, the reciprocal angles $\phi = 0°$ and $\phi = 90°$ correspond to the respective directions x and y in a membrane plane.

Number of Repetitive Units. In many periodic problems, a minimum of ~5 periods per problem dimension is usually required to reproduce experimentally the physical results related to the infinite problem with a low truncating error. For instance, in diffractive optics, at least 4 (in x) × 4 (in y) = 16 periods of a 2D periodic spatial-hologram profile (which can be fabricated by lithography or etching in a SiO_2 plate) are needed to reconstitute its (X, Y) far-field image from a unique 2D Fourier transform with a low aliasing error between the discrete diffraction orders (26). In the presented study, the spatial repetition in the dimension y is intrinsically infinite due to nanodot elongation in y. Only the dimension x is necessary to estimate experimentally the required number of periods needed to measure the thermal conductivity of the infinite membrane. Moreover, the thin nanomaterial is proposed for possible applications in microdevices (see Introduction). From the precedent, a possible length $L_x \geq 1$ μm of the membrane between the junctions in the direction x is realistic. However, the supercell length is $d_x = 30\ a = 16.293$ nm in x for "Template 1" (Figure 1c). In this case, at least 1000/16.293 ≈ 61 repetitive units would affect a heat flux propagating between the junctions in x. This number is ~12 folds larger than 5. Consequently, considering an infinite membrane is reliable in the proposed model.

Supporting Information Available: Mathematical demonstrations of eqs 1 and 2 are given in parts A and B (PDF). This material is available free of charge via the Internet at http://pubs.acs.org.

REFERENCES AND NOTES

(1) Guise, O.; Yates, J. T., Jr.; Levy, J.; Ahner, J.; Vaithyanathan, V.; Scholm, D. G. *Appl. Phys. Lett.* **2005**, *87*, 171902.
(2) Voigtländer, B. *Surf. Sci. Rep.* **2001**, *43*, 127–254.
(3) Rothemund, P. W. K. *Nature* **2006**, *440*, 297–302.
(4) Chen, D.; Wang, X.; Liu, T.; Wang, X.; Li, J. *ACS Appl. Mater. Interfaces* **2010**, *2*, 2005–2011.
(5) Alvarez, N. T.; Orbaek, A.; Barron, A. R.; Tour, J. M.; Hauge, R. H. *ACS Appl. Mater. Interfaces* **2010**, *2*, 15–18.
(6) Tseng, T.-K.; Choi, J.; Jung, D.-W.; Davidson, M.; Holloway, P. H. *ACS Appl. Mater. Interfaces* **2010**, *2*, 943–946.
(7) Tzeng, Y.-F.; Wu, H.-C.; Sheng, P.-S.; Tai, N.-H.; Chiu, H.-T.; Lee, C.-Y.; Lin, I.-N. *ACS Appl. Mater. Interfaces* **2010**, *2*, 331–334.
(8) Gillet, J.-N. *Appl. Phys. Express* **2010**, in press.
(9) Gillet, J.-N. In *Best Scientific Paper, Proceedings of the 28th International Conference on Thermoelectrics, ICT 2009*; Freiburg, Germany, July 26−30, 2009; IEEE: Piscataway, NJ, 2009.
(10) Gillet, J.-N.; Volz, S. *J. Electron. Mater.* **2009**, *39*, 2154–2161.
(11) Gillet, J.-N.; Chalopin, Y.; Volz, S. *ASME J. Heat Transfer* **2009**, *131*, 043206.
(12) Venkatasubramanian, R.; Siivola, E.; Colpitts, T.; O'Quinn, B. *Nature* **2001**, *413*, 597–602.
(13) Chowdhury, I.; Prasher, R.; Lofgreen, K.; Chrysler, G.; Narasimhan, S.; Mahajan, R.; Koester, D.; Alley, R.; Venkatasubramanian, R. *Nat. Nanotech.* **2009**, *4*, 235–238.
(14) Gillet, J.-N.; Degorce, J.-Y.; Meunier, M. *Appl. Phys. Lett.* **2005**, *86*, 222104.
(15) Majumdar, A. *Nat. Nanotechnol.* **2009**, *4*, 214–215.
(16) Blazej, R.; Kumaresan, P.; Mathies, R. A. *Proc. Natl. Acad. Sci.* **2006**, *103*, 7240–7245.
(17) El-Ali, J.; Sorger, P. K.; Jensen, K. F. *Nature* **2006**, *442*, 403–411.
(18) Geissler, M.; Roy, E.; Diaz-Quijada, G.-A.; Galas, J.-C.; Veres, T. *ACS Appl. Mater. Interfaces* **2009**, *1*, 1387–1395.
(19) Chalopin, Y.; Gillet, J.-N.; Volz, S. *Phys. Rev. B* **2008**, *77*, 233309.
(20) Bohren, C. F., Huffman, D. R. *Absorption and Scattering of Light by Small Particles*; Wiley: New York, 1998.
(21) van de Hulst, H. C. *Light Scattering by Small Particles*; Dover:New York, 1981.
(22) Kim, W.; Majumdar, A. *J. Appl. Phys.* **2006**, *99*, 084306.
(23) Glassbrenner, C. J.; Slack, G. A. *Phys. Rev.* **1964**, *134*, A1058–A1069.
(24) Goldsmid, H. J. In *CRC Handbook of Thermoelectrics*; Rowe, D. M., Ed.; CRC Press: Boca Raton, FL, 1992; pp 19−26.
(25) Hochbaum, A. I.; Chen, R.; Delgado, R. D.; Liang, W.; Garnett, E. C.; Najaran, M.; Majumdar, A.; Yang, P. *Nature* **2008**, *451*, 163–167.
(26) Gillet, J.-N. Eléments Optiques Diffractifs Conçus avec des Ouvertures Trapézoïdales et Polygonales et de Nouveaux Algorithmes d'Optimisation. Ph.D. dissertation, Université Laval, Québec, Canada, 2001; pp 108−112.

AM1006518